Available online at www.sciencedirect.com
ScienceDirect
International Journal of Thermal Sciences 48 (2009) 590–601
International Journal of Thermal Sciences
www.elsevier.com/locate/ijts

A numerical investigation of flow and heat transfer in rotating U-shaped square ducts

M.R.H. Nobari *, A. Nousha [1], E. Damangir [2]

Department of Mechanical Engineering, Amirkabir University of Technology, 424 Hafez Ave., P.O. Box 15875-4413, Tehran, Iran

Received 4 April 2007; received in revised form 15 April 2008; accepted 17 April 2008

Available online 19 May 2008

Abstract

Three-dimensional incompressible viscous flow and heat transfer in a rotating U-shaped duct with a square cross-section are studied numerically. The governing equations including full Navier–Stokes and energy equations are solved using a finite volume method based on the SIMPLER algorithm in an orthogonal uniform grid. The effects of wall curvature and rotation on the flow field and heat transfer considering different directions of rotation are presented in detail. The results show that in the bend region, the centrifugal forces due to curvature are significant, performing an intensive outward secondary flows resulting in an increase of heat transfer on the outer wall. But in the straight parts of the duct, secondary flows due to Coriolis forces are dominant. The comparison of numerical results at different rotation angles indicates that the maximum heat transfer rate occurs when the duct rotates about an axis parallel to the axis of duct curvature, at which both the Coriolis and the centrifugal forces intensify each other, while the minimum heat transfer rate takes place in the negative diagonal axis of rotation with angles of $\alpha = 180$ and $\beta = 135$.

© 2008 Elsevier Masson SAS. All rights reserved.

Keywords: Rotating channel; U-shaped duct; Incompressible viscous flow; Heat transfer

1. Introduction

Fluid flow and heat transfer in rotating ducts occur in many engineering applications such as cooling in electrical machineries, gas turbine blades and other rotating systems. Understanding rotational effects on the flow and heat transfer helps to improve design of those devices.

Orthogonal rotation in straight pipes and ducts has been widely studied before. Fluid flow and heat transfer for various geometries have been discussed by Shah and London [1] for stationary ducts. Speziale [2,3] used a finite difference stream function vorticity method to study laminar flow in a long straight rectangular duct under orthogonal rotation. Soong [4,5] set up heat transfer measurements in rotating isothermal rectangular ducts for aspect ratios of 0.2, 0.5, 1, 2, and 5, Reynolds numbers ranging from 717 to 16000 and rotational Reynolds numbers from 20 to 320. Jen and Lavine [6] numerically analyzed laminar forced convection in the entrance region of an isothermal square duct rotating about an axis perpendicular to the duct axis. They solved vorticity transport equations numerically using the power-law scheme and presented secondary flows, axial velocity and temperature contours in the entrance region at three different independent parameters consisting of Prandtl number (Pr), a combined Reynolds and rotational Reynolds number ($Re{\cdot}Re_\Omega$), and Rossby number ($Ro = Re/Re_\Omega$). Mahadevappa and Rao [7] have done a numerical study of steady laminar fully developed flow and heat transfer in rectangular and elliptical ducts rotating about an axis parallel to the duct axis. They used a finite-difference method and presented correlations for heat transfer in rotating rectangular and elliptical ducts, indicating that elliptical geometry is superior to the others that are frequently used as coolant channels in rotating machinery.

Dean [8], for the first time, studied the secondary flow in the curved pipe by introducing a single parameter, K, called the Dean Number, which is defined as $Re\sqrt{D/R_0}$. Hwang and

* Corresponding author.
E-mail address: mrnobari@aut.ac.ir (M.R.H. Nobari).
[1] Graduate Student.
[2] Assistant Professor.

1290-0729/$ – see front matter © 2008 Elsevier Masson SAS. All rights reserved.
doi:10.1016/j.ijthermalsci.2008.04.001

Nomenclature

a	acceleration
C_f	skin friction
D	hydraulic diameter
K	Dean Number
L_{en}	dimensionless entrance length
L_X, L_Y, L_Z	dimensionless lengths of duct in x, y, and z directions
Nu	Nusselt number
Pr	Prandtl number
R_C	circular bend inner radius
Re	Reynolds number
Re_Ω	rotational Reynolds number
Ro	Rossby number
S	axial distance of the duct
T	dimensionless temperature
x, y, z	dimensionless independent variables
V	velocity vector

Greek symbols

α	angle with respect to x–y plane
β	angle with respect to x–z plane
υ	kinematic viscosity
ρ	density
τ_w	wall shear stress
Ω	rotational velocity

Subscripts

in	inlet variables
x, y, z	components in x, y and z directions
wall	duct wall
en	entrance length
mean	mean inlet and outlet variable

Superscripts

$*$	dimensional variables

Lai [9,10] studied three-dimensional flow problems in rotating multi-pass square channels. Most recently Papa [11] has studied flow field and heat transfer in circular and square channels with a sharp 90 degree bend rotating about an axis parallel to the axis of the inlet of channel. In another work, Papa [12] obtained numerical results for developing laminar flow in ducts having circular or square cross-sections and a 180 degree bend rotating either positively or negatively about an axis parallel to the axis of curvature of the duct.

In this paper, a numerical simulation based on the SIMPLER finite volume method is performed to study developing incompressible flow and heat transfer through a U-shaped duct with a square cross-section considering isothermal boundary condition at the walls. Previous studies on this subject are limited to the rotational axis perpendicular or parallel to the axial flow direction. Here, seven different major rotational directions are taken into account to study in detail the effects of rotational direction on the flow field pattern and consequently on the friction coefficient and heat transfer rate in a U-shaped duct.

2. Governing equations

Fig. 1 shows the geometry of the channel, where the inlet velocity is parallel to the z-axis (axis of duct) and radially outward. The length of the straight parts of the channel is 9 times of hydraulic diameter, D. At the end of the first straight passage, flow enters the 180 degree circular bend region with the inner radius of $R_c = 1.25D$, then passes radially inward through the second straight part.

The direction of rotation can be shown by its vector components, or by its corresponding angles α and β relating to x–y and x–z planes, respectively.

As shown in Fig. 1, two parallel walls of the duct are denoted as the top and the bottom walls and other two walls are denoted the inner and the outer walls.

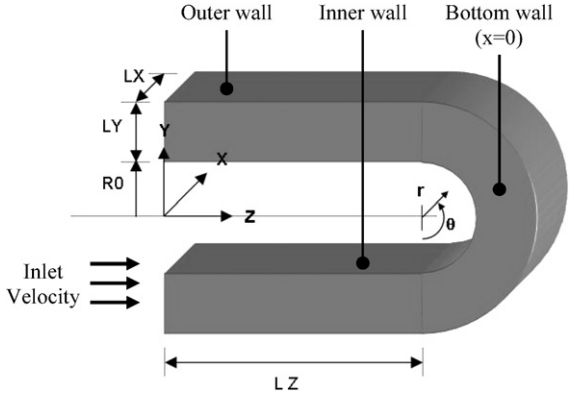

Fig. 1. Geometry of the duct and coordinate systems.

The governing equations used to study the flow and heat transfer in a rotating U-shaped square duct for incompressible flow in a rotating coordinate system include two kinds of coordinate systems, the Cartesian coordinates for two straight parts of channel and the cylindrical one for bend region.

Using the following non-dimensional parameters

$$a = \frac{D \cdot a^*}{w_{in}^{*2}}, \quad u = \frac{u^*}{w_{in}^*}, \quad v = \frac{v^*}{w_{in}^*}, \quad w = \frac{w^*}{w_{in}^*}$$

$$L_X = \frac{L_X^*}{D}, \quad L_Y = \frac{L_Y^*}{D}, \quad L_Z = \frac{L_Z^*}{D}$$

$$Re_\Omega = \frac{\Omega \cdot D^2}{\nu}, \quad K = Re\sqrt{\frac{D}{R_C}}, \quad Ro = \frac{\Omega \cdot D}{w_{in}^*}$$

$$Re = \frac{w_{in}^* \cdot D}{\nu}, \quad p = \frac{p^*}{\rho w_{in}^{*2}}, \quad T = \frac{T^* - T_{in}^*}{T_{wall}^* - T_{in}^*}$$

the dimensionless governing equations in a Cartesian coordinate system are as follows

$$\frac{\partial u}{\partial x} + \frac{\partial v}{\partial y} + \frac{\partial w}{\partial z} = 0 \tag{1}$$

$$\frac{\partial u^2}{\partial x}+\frac{\partial uv}{\partial y}+\frac{\partial uw}{\partial z} = -\frac{\partial p}{\partial x}+\frac{\partial}{\partial x}\left(\frac{1}{Re}\frac{\partial u}{\partial x}\right) + \frac{\partial}{\partial y}\left(\frac{1}{Re}\frac{\partial u}{\partial y}\right)+\frac{\partial}{\partial z}\left(\frac{1}{Re}\frac{\partial u}{\partial z}\right)+a_x \tag{2}$$

$$\frac{\partial uv}{\partial x}+\frac{\partial v^2}{\partial y}+\frac{\partial vw}{\partial z} = -\frac{\partial p}{\partial y}+\frac{\partial}{\partial x}\left(\frac{1}{Re}\frac{\partial v}{\partial x}\right)+\frac{\partial}{\partial y}\left(\frac{1}{Re}\frac{\partial v}{\partial y}\right) + \frac{\partial}{\partial z}\left(\frac{1}{Re}\frac{\partial v}{\partial z}\right)+a_y \tag{3}$$

$$\frac{\partial uw}{\partial x}+\frac{\partial vw}{\partial y}+\frac{\partial w^2}{\partial z} = -\frac{\partial p}{\partial z}+\frac{\partial}{\partial x}\left(\frac{1}{Re}\frac{\partial w}{\partial x}\right) + \frac{\partial}{\partial y}\left(\frac{1}{Re}\frac{\partial w}{\partial y}\right)+\frac{\partial}{\partial z}\left(\frac{1}{Re}\frac{\partial w}{\partial z}\right)+a_z \tag{4}$$

$$\frac{\partial uT}{\partial x}+\frac{\partial vT}{\partial y}+\frac{\partial wT}{\partial z} = \frac{\partial}{\partial x}\left(\frac{1}{Re\cdot Pr}\frac{\partial T}{\partial x}\right)+\frac{\partial}{\partial y}\left(\frac{1}{Re\cdot Pr}\frac{\partial T}{\partial y}\right) + \frac{\partial}{\partial z}\left(\frac{1}{Re\cdot Pr}\frac{\partial T}{\partial z}\right) \tag{5}$$

where, the starred variables are dimensional ones, L_x, L_y and L_z are dimensions of the straight parts of the duct (as shown in Fig. 1), u, v, w are velocity components and a_x, a_y, a_z are acceleration components in the x-, y-, and z-directions, respectively. p denotes pressure and T temperature, and Pr the Prandtl number.

The centrifugal and Coriolis resultant acceleration in dimensionless vector form is

$$a = -Ro\times(Ro\times r)-2Ro\times V \tag{6}$$

3. Numerical method

A cell-centered finite volume method based on SIMPLER algorithm [13,14] is employed to solve the steady state governing equations. A power-law scheme is used to calculate the coefficients of convection and diffusion fluxes through the interfaces. For mesh generation of the physical domain, the duct is split into two straight and one bend regions, where uniform staggered cubic and cylindrical control volumes are used for two straight parts and bend region, respectively. By this staggered grid, the velocity components are calculated at points that lie on the faces of the main control volumes.

Using SOR iterative scheme, the maximum relative error for the convergence of solution is set to be less than 10^{-5}.

Table 1
A comparison of $C_f\,Re$ and Nu in the straight rectangular duct

Re	$C_f\,Re$			Nu		
	This work	Shah [1]	% Difference	This work	Shah [1]	% Difference
100	14.090	14.23	0.98	2.986	2.98	0.20
200	14.164		0.46	2.989		0.30
500	14.377		1.03	3.012		1.07

3.1. Boundary conditions

In this work, the inlet temperature and velocity profiles are considered uniform.

$$u_{\text{in}} = v_{\text{in}} = 0, \qquad w_{\text{in}} = 1, \qquad T_{\text{in}} = 0 \tag{7}$$

At the walls, no-slip condition is used for velocity components and the temperature of all the walls is considered to be constant at $T_{\text{wall}} = 1$.

No boundary conditions are required for pressure at the inlet and walls. Since at these boundaries, which are the faces of corresponding pressure control volumes, the real values of velocity vectors are known and there is no appearance of outside neighbor node in derivation of Poisson equation of pressure (or the coefficient of this neighbor node is zero). More details of the boundary conditions for pressure are discussed by Patankar [13].

At the exit of duct, the Neumann condition of zero-gradient is used, and the temperature is exponentially extrapolated so that the Nusselt number remains constant at the exit of the duct.

3.2. Validation of the numerical method

Flow and heat transfer in the stationary straight rectangular duct are simulated numerically in order to validate the accuracy the code developed here. The length of the duct is chosen longer than the dimensionless hydrodynamic entrance length denoted by L_{en} to ensure the fully developed flow at the exit of the duct. The Sparrow integral solution [15] predicts the value of $L_{\text{en}}/Re = 0.0065$ for the laminar entrance length, and Schlichting [16] predicts $L_{\text{en}}/Re = 0.04$ by obtaining a series solution. The value of $L_{\text{en}} = 30$ has been chosen for the Re range from 100 to 500. Table 1 shows the numerical results for the friction factors and Nusselt numbers at different Reynolds numbers. The comparison with the numerical results obtained by Shah and London [1] indicates a very good agreement.

3.3. Grid independency test

A grid independency study is performed using three different uniform staggered grids of $10\times10\times110$, $20\times20\times110$, and $24\times24\times150$. The mean Nusselt number is used as a parameter to check the grid independency of the results, which is shown in Fig. 2 for the stationary U-shaped square duct at Reynolds number of 200. The comparison of the three grid results indicates the grid independency of the numerical code implemented here. It should be mentioned that all runs considered in this work are carried out in a grid size of $20\times20\times110$ ($20\times20\times40$ for the straight parts and $20\times20\times30$ for the bend region).

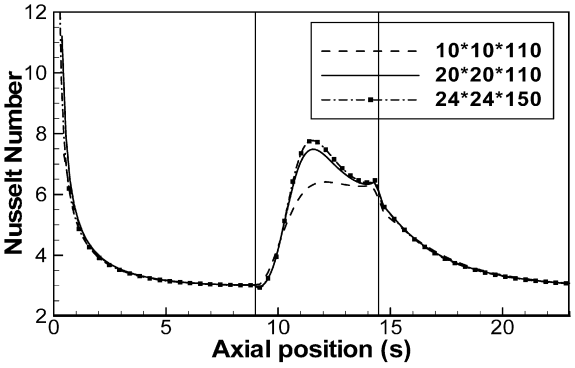

Fig. 2. Grid independency test at $Re = 200$.

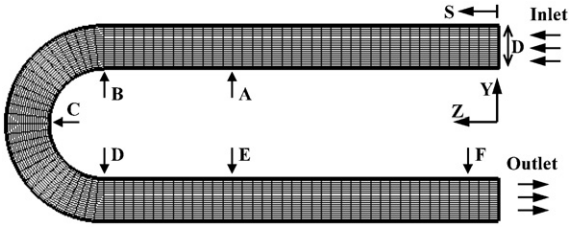

Fig. 3. Symmetry plane of the duct and main grids. Section A: $S/D = 6.075$ ($z = 6.075$), section B: $S/D = 9$ ($z = 9$), section C: $S/D = 11.75$ (mid-section of Bend), section D: $S/D = 14.5$ ($z = 9$), section E: $S/D = 17.423$ ($z = 6.075$), section F: $S/D = 22.56$ ($z = 0.9$).

4. Results and discussion

Here, the effects of the magnitude and direction of rotation as well as the bend of the U-shaped duct on the flow field and heat transfer are studied in detail. Fig. 3 shows a view of symmetry plane and grid distribution of the duct where the most suitable cross sections of A, B, C, D, E and F are chosen to show the flow and temperature field patterns inside the duct.

4.1. Velocity and temperature fields

To investigate the physical aspects of fluid flow and heat transfer in the U-shaped duct, the velocity and temperature fields are taken into account at $Re = 200$ for the stationary duct and the duct with two rotation numbers of $Ro = 0.1$ and 0.2 at seven different directions of rotation defined in Table 2 by the two angles of α and β.

In Figs. 4, 5, and 6, the non-dimensional secondary velocity fields, axial velocity and temperature contours are shown respectively for eight different cases specified in Table 2. In each case, the velocity and temperature fields are illustrated at the six different selected cross-sections of the duct specified in Fig. 3. Except for case 1 which indicates the stationary duct, in all other cases the rotation number is fixed at $Ro = 0.2$.

In the entrance region of the first straight passage of case 1, the axial velocity profile approaches a parabolic profile (Fig. 4A), but in the bend region, centrifugal forces generated due to the curvature produce two counter-rotating vortices (Fig. 4C). These vortices causes the core fluid moves towards the outer wall and consequently the peak of the axial velocity shifts from the center of the duct towards the outer wall, resulting in the thinner boundary layer on the outer and thicker boundary layer on the inner wall. This is accompanied with a pressure increase on the outer and a pressure decrease on the inner wall. The resulting secondary flows begin at the entrance of the bend region (section B), intensify at the midsection (section C), gradually weaken at the downstream (section D), and finally vanish in the second straight passage (section E). Again at the outlet, the flow approaches the fully developed condition (section F). The corresponding axial flow velocity and temperature contours are shown in Figs. 5 and 6, where it can be easily observed that a thin (thick) hydrodynamic and thermal boundary layers appears at the outer (inner) wall in the bend region, where the heat transfer rate is higher (lower) than the straight part of the pipe. However, both of the boundary layers at the top and the bottom walls become thinner in the bend region and the axial velocity profile flattens.

Case 2 in Figs. 4–6 is related to the duct rotating positively about x-axis ($\alpha = 0$ and $\beta = 0$). This case of rotation is called "positive rotation" where the centrifugal and Coriolis forces strengthen the effect of each other in the bend region and the symmetry plane of the duct (plane of $x = 0.5$) coincides with the symmetry plane of flow field. The Coriolis forces in this case generate two symmetrical counter-rotating vortices in the first and second passages of duct, which are at the same direction of the vortices generated by the centrifugal forces. These vortices cause the core fluid to move towards the outer wall in all over the duct and the maximum temperature and the axial velocity shifts from the center towards outer wall. In this case and all other rotational cases, the secondary flow mostly is governed by the Coriolis forces causing the boundary layer to get thinner at the outer wall and thicker at the inner wall.

In case 3, the duct rotates negatively about x-axis ($\alpha = 180$ and $\beta = 180$), where the Coriolis forces acting in the opposite direction comparing with case 2 generate two symmetrical counter-rotating vortices in the first and second straight passages of the duct and move the core fluid towards the inner wall to increase heat transfer rate and friction over it. In this case, the axial velocity peak moves from the center toward inner wall due to Coriolis forces, but in the bend region, the centrifugal forces become dominant and perform the vortices in the opposite direction of those generated in the first passage. Downstream of the bend region, these vortices vanish gradually and again the Coriolis forces govern the flow pattern in the second straight passage.

To investigate further the effect of rotation direction change on the flow and temperature field, case 4 is taken into account when the duct rotates about y-axis ($\alpha = 90$ and $\beta = 0$). In this case, the top wall ($x = 1$) is the leading and the bottom wall ($x = 0$) is the trailing surface. In the first straight passage (section A), the Coriolis forces generate two counter-rotating vortices enforcing the core fluid towards the trailing (high pressure) wall and shifting the maximum axial velocity and minimum temperature towards it. But, in the bend region, the flow pattern deforms due to dominant centrifugal forces resulting in a large vortex near the leading and a small one near the trailing wall (sections B, C, and D). Here, the maximum axial velocity and the minimum temperature of the fluid moves near the

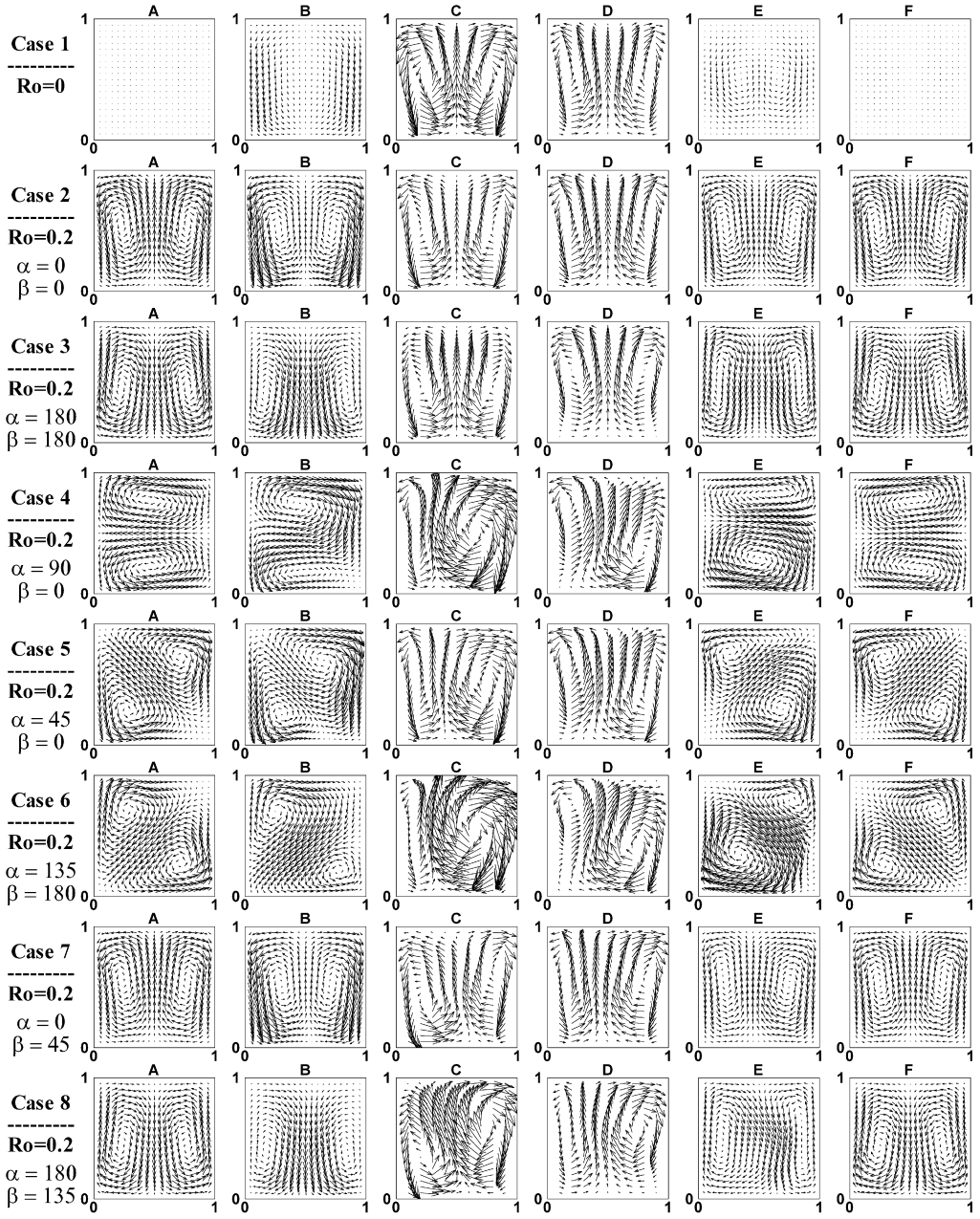

Fig. 4. Secondary flow field in cross sections A–F of the stationary and rotating U-shaped square duct about seven different axes at $Re = 200$. Top (outer wall), bottom (inner wall), left (bottom wall), right (top wall).

outer wall at the corner close to the trailing wall. In the second straight passage (sections E and F) the direction of Coriolis forces are reversed, creating two vortices which move the core fluid towards the leading wall in contrast to the first passage.

The duct rotation about the axis of $y = +x$ ($\alpha = 45$ and $\beta = 0$) is considered in case 5. In this case, Coriolis forces act in diagonal direction of the duct cross-section, generating two counter-rotating triangular vortices in each of the first and second passages. The velocity and temperature contours show that the cold fluid with high velocity moves near the outer bottom corner of the first passage, but in the second passage it occurs near the outer top corner of the second passage due to reversing the Coriolis forces direction and generation of the vortices at the opposite corners. A similar pattern is observed in case 6 which corresponds to the rotation about the axis of $y = -x$ ($\alpha = 135$ and $\beta = 180$). In either of the two cases as well as case 4, the resultant effect of the centrifugal and Coriolis forces in the bend region (section C) deforms symmetric counter rotating vortices into a large and a small ones.

Rotation in x–z plane is studied considering two other orientations of $z = +x$, where $\alpha = 0$ and $\beta = 45$ (case 7), and $z = -x$, where $\alpha = 180$ and $\beta = 135$ (case 8). Secondary flow patterns in these two cases are similar to cases 2 and 3, respectively, but there is a minor clockwise deviation of contours in the bend region of the duct (sections C and D).

By increasing the rotation number in all the above mentioned cases, the near wall velocity and temperature gradients increase, the peak points of the velocity and temperature profiles move

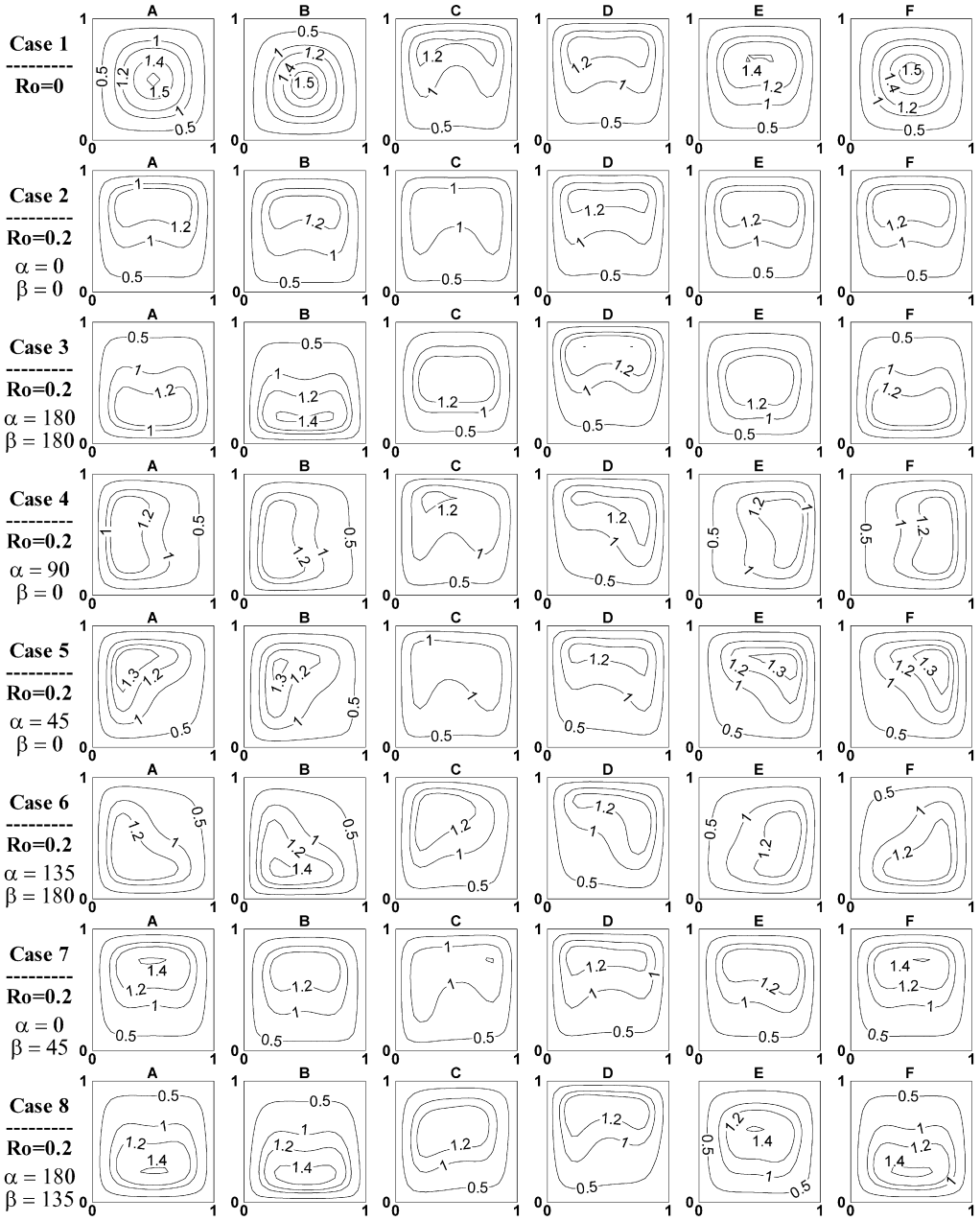

Fig. 5. Dimensionless axial velocity contours in cross sections A–F of the stationary and rotating U-shaped square duct about seven different axes at $Re = 200$. Top (outer wall), bottom (inner wall), left (bottom wall), right (top wall).

far away from the center, the velocity profile flattens more, and the outlet mean temperature increases.

Furthermore, by increasing the Reynolds number from 200 to 500 and 1000, the strength of vortices and the ratio of Coriolis to Centrifugal forces increase, four or six vortices in sections C and D are generated, the axial velocity profile flattens, and the outlet mean temperature decreases.

4.2. Skin friction and heat transfer

Since friction factor and Nusselt number are two of the most important flow parameters, the product of the peripherally averaged friction factor and the Reynolds number, $C_f\,Re$, and the average Nusselt numbers on the walls along with the peripherally averaged Nusselt numbers are presented numerically. The typical flow and temperature fields shown for the eight cases in Figs. 4–6 are helpful in better understanding some physical points behind the friction factor and heat transfer coefficient variations. Here, the friction factor is defined as

$$C_f = \frac{2\bar{\tau}_w}{\rho w_{\text{in}}^{*2}} \tag{8}$$

where $\bar{\tau}_w$ is the peripherally averaged wall shear stress and can be calculated using local derivative as follows

$$C_f = \frac{2\partial\bar{w}/\partial n|_{\text{wall}}}{Re} \tag{9}$$

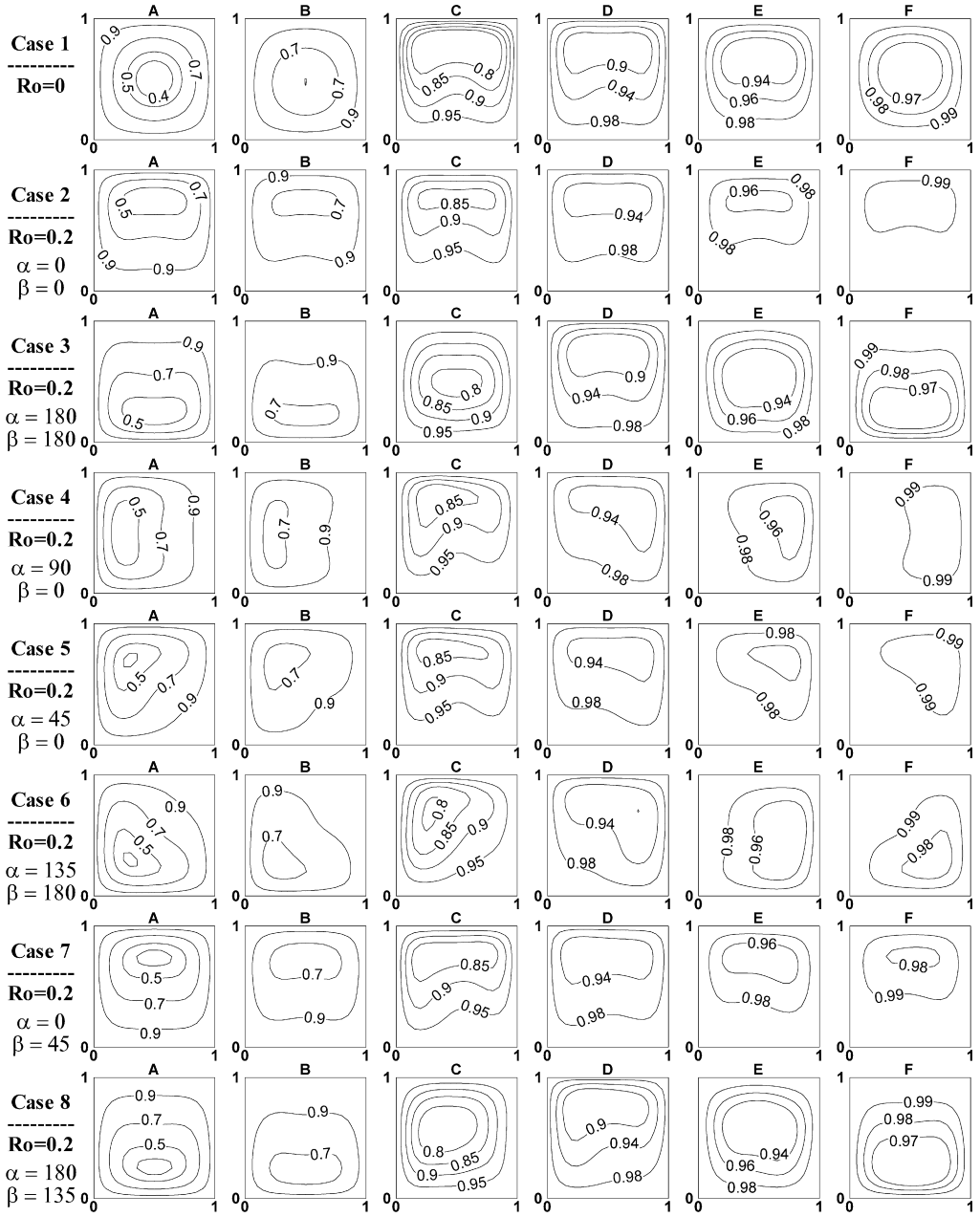

Fig. 6. Dimensionless temperature contours in cross sections A–F of the stationary and rotating U-shaped square duct about seven different axes at $Re = 200$. Top (outer wall), bottom (inner wall), left (bottom wall), right (top wall).

Table 2
Different cases of rotation

Case no.	1	2	3	4	5	6	7	8
Axis of rotation			$-x$	$-x$	y	$y=x$, $z=0$	$y=-x$, $z=0$	$z=x$, $y=0$	$z=-x$, $y=0$
α (degree)	–	0	180	90	45	135	0	180
β (degree)	–	0	180	0	0	180	45	135

To study the friction factor in the rotating duct, the peripherally averaged values of $C_f\,Re$ versus dimensionless axial distance S/D for the stationary and positive rotation cases at three different Reynolds numbers are shown in Fig. 7. The comparison of the numerical results indicates that at a fixed amount of S/D, the $C_f\,Re$ increases proportional to the Re and Ro all over the duct, except in the bend region where the effect of rotation number is small on the $C_f\,Re$ curve. Fig. 8 shows the same results in the case of negative rotation ($\alpha = \beta = 180$), where similar to the previous case the $C_f\,Re$ increases as Re and Ro increase through the duct, but some oscillation behavior appears in the second straight passage and in the bend region where a relative minimum value inside and two relative max-

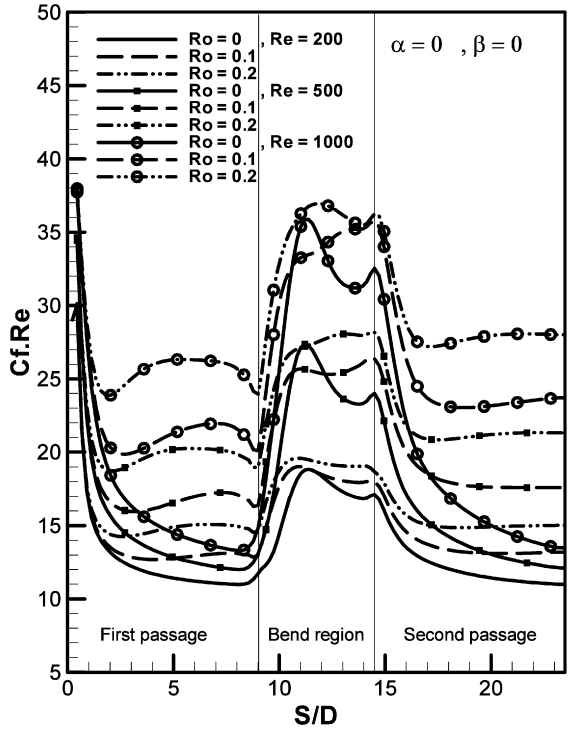

Fig. 7. $C_f\,Re$ versus axial distance of the duct in positive rotation about x-axis ($\alpha = 0$, $\beta = 0$).

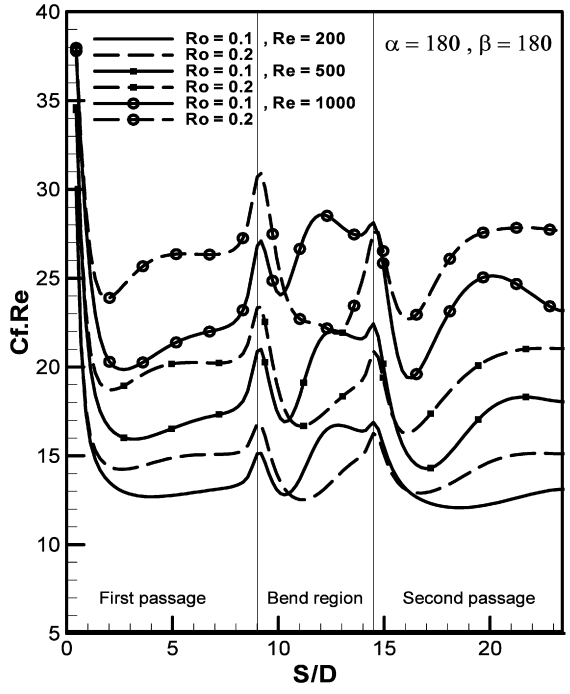

Fig. 8. $C_f\,Re$ versus axial distance of the duct in negative rotation about x-axis ($\alpha = 180$, $\beta = 180$).

imum values at the ends are distinguished by a forty percent decrease in skin friction comparing with the corresponding positive rotation cases. This can be easily deduced by considering the typical flow fields shown in Figs. 4–6 for the corresponding cases. As it is clear, in the positive rotation case the centrifugal and Coriolis forces act at the same direction in the bend region and strengthen the secondary flow effects, which is followed by a friction factor increase in the bend region comparing with the stationary case. But in the negative rotation case, the reverse occurs and the centrifugal and Coriolis forces act in the opposite direction in the bend region. This weakens the secondary flow effects and decreases the friction factor values in the bend region comparing with those in the stationary case (see sections B, C, D in Fig. 4).

Now, the effects of different rotation directions on the heat transfer rate are studied in Figs. 9–12, where the peripherally averaged Nusselt numbers and the average Nusselt numbers on the four side walls versus the axial direction of the duct are illustrated at different rotation numbers for $Re = 200$ including $Ro = 0$. In the entrance of the stationary case, due to the thin boundary layer, the heat transfer rate is high, but downstream, the average Nusselt number of the duct decreases and approaches the fully developed value. Because of formation of secondary flows in the bend region, the average Nusselt number increases as twice as its value in the first straight passage. Again in the second straight passage, as the secondary flows vanish, the Nusselt number gradually decreases to the fully developed value. In the stationary case, the Nusselt numbers on the four side walls are identical in the first straight passage, but in the bend region, a higher Nusselt number on the outer wall (about three times of its value before the bend region) appears due to the sharp temperature gradient generated by the centrifugal forces on this surface. For the same reason, higher values of the Nusselt numbers on the top and bottom walls of the bend region appear, twice as much as the straight passage values. However, the centrifugal forces retard the fluid flow on the inner wall and thicken the thermal boundary layer which reduces the heat transfer rate about half of the one in the straight passage. This physical effects of the centrifugal forces on making thinner or thicker the hydrodynamic or thermal boundary layers in the bend region can be easily seen in Figs. 4–6 at cross-section C.

In all cases of rotation, the average Nusselt numbers in the straight parts of the duct are higher than the stationary one because of the existence of the Coriolis forces. This increase of Nusselt number is almost proportional to the rotation number. But, when the rotation vector has a component parallel to the axis of duct ($\beta \neq 0, 180$), due to reduced Coriolis forces the average Nusselt number is lower than the other rotational cases. In the bend region, the Nusselt number does not change proportional to the rotation number, however, it converges to a certain value at the bend outlet. Furthermore, the Nusselt number is very sensitive to the direction of rotation. When $\alpha, \beta > 90$, the Coriolis forces act opposite to the centrifugal forces in the bend region and counter-balance each other. This phenomenon moves the cold fluid toward the core of the duct and thickens the boundary layer which results in the reduction of the Nusselt number at the inlet of the bend region. Beyond the mid-section of the bend region, the Coriolis forces has dominant role in the generation of secondary flows, and hence the average Nusselt number starts increasing again.

To get more insight into the rotation direction effect on the heat transfer, two positive and negative rotation directions are illustrated in Figs. 9 and 10, respectively. As it is clear from

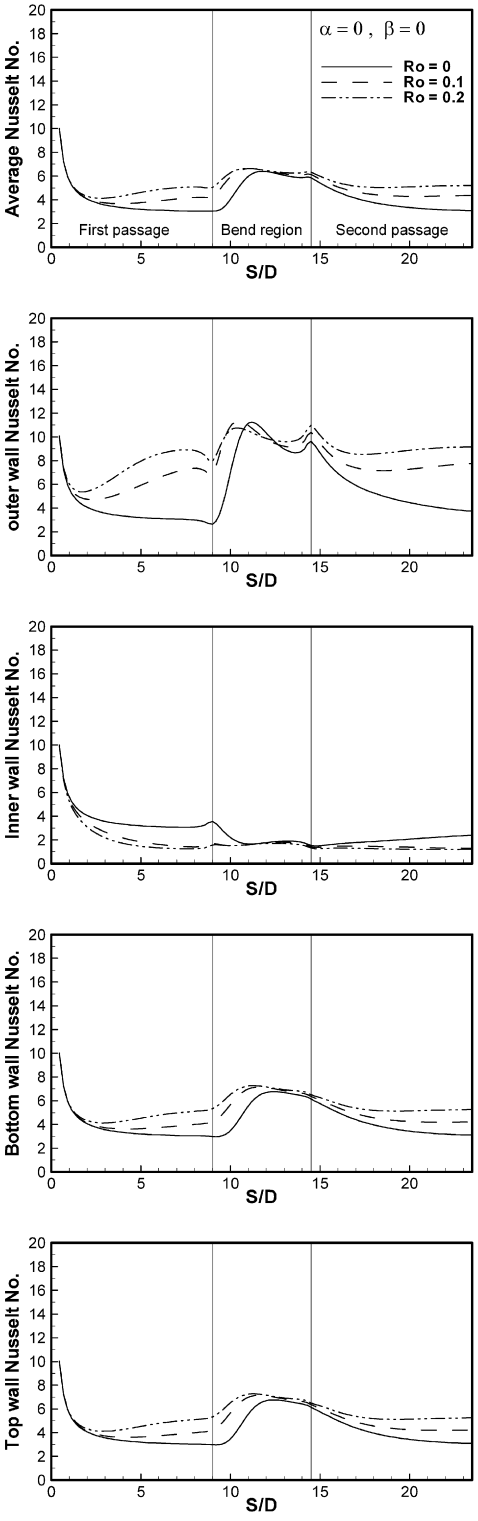

Fig. 9. Average peripheral Nusselt number and each four wall Nusselt number of the duct versus axial distance at $Re = 200$ for rotation axis at angles of $\alpha = 0$ and $\beta = 0$.

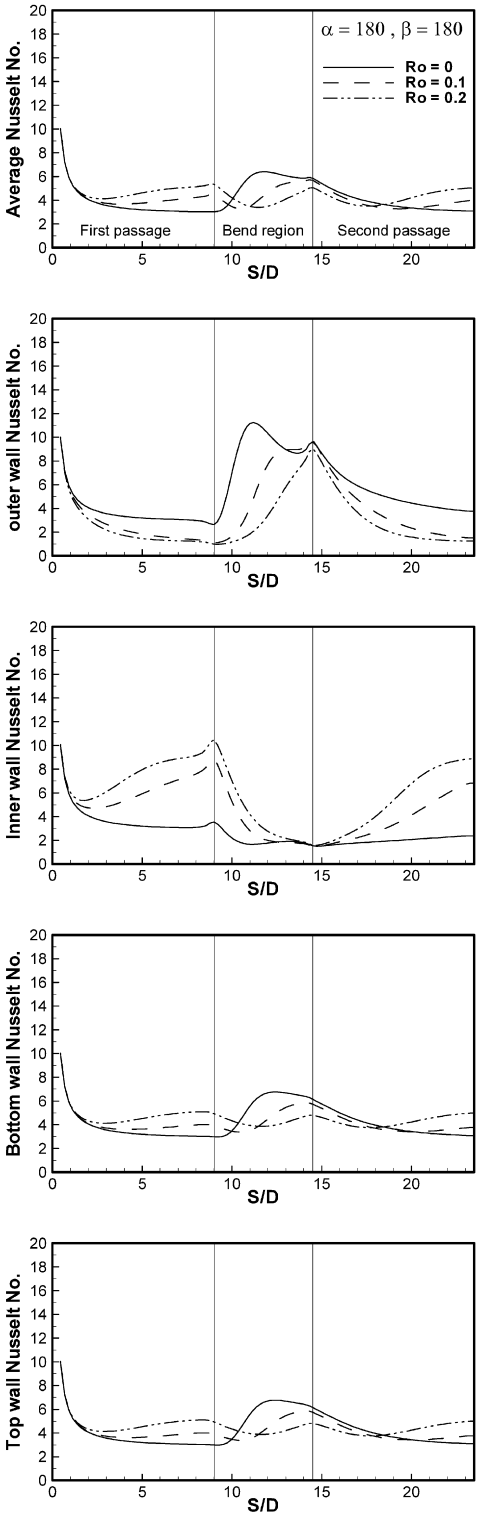

Fig. 10. Average peripheral Nusselt number and each four wall Nusselt number of the duct versus axial distance at $Re = 200$ for rotation axis at angles of $\alpha = 180$ and $\beta = 180$.

Fig. 9, in the positive rotation the heat transfer rate is larger than the stationary duct on the outer wall due to the thin thermal boundary layer generated by the strengthened secondary flow effects and lower than that on the inner wall due to thick thermal boundary generated for the same reason. However, the Nusselt numbers on the top and bottom walls proportionally increase with rotation number. Reverse effects occur in the negative rotation (Fig. 10), where the inner wall has a larger and the outer wall has a lower value of the Nusselt number. The top and bottom walls behaves similar to the positive rotation except in

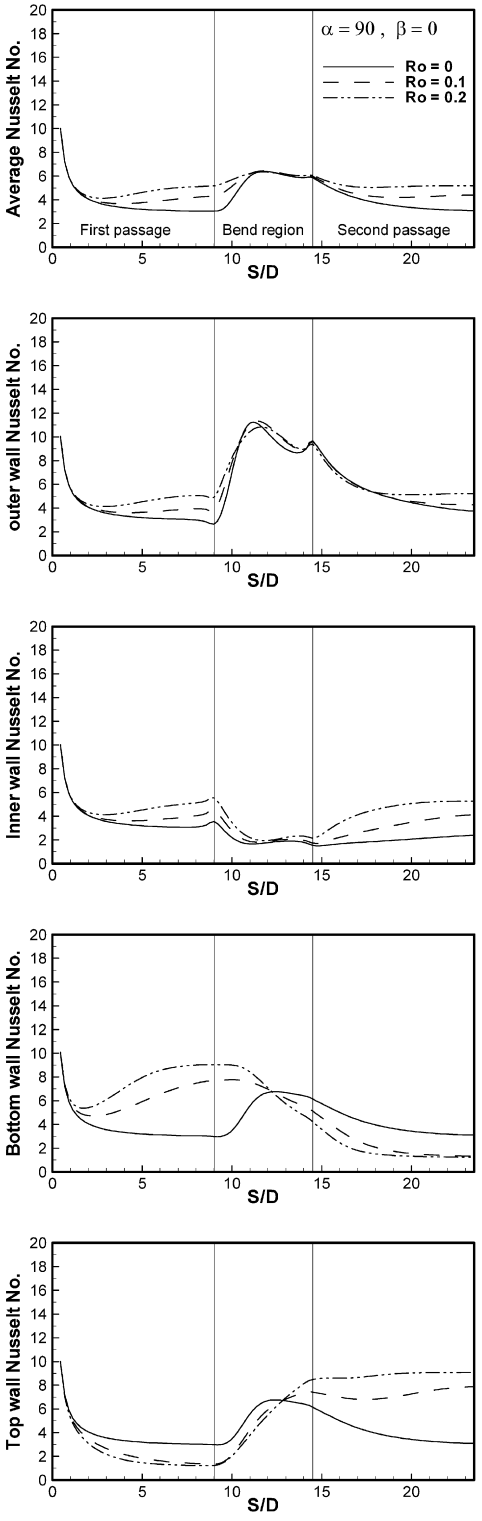

Fig. 11. Average peripheral Nusselt number and each four wall Nusselt number of the duct versus axial distance at $Re = 200$ for rotation axis at angles of $\alpha = 90$ and $\beta = 0$.

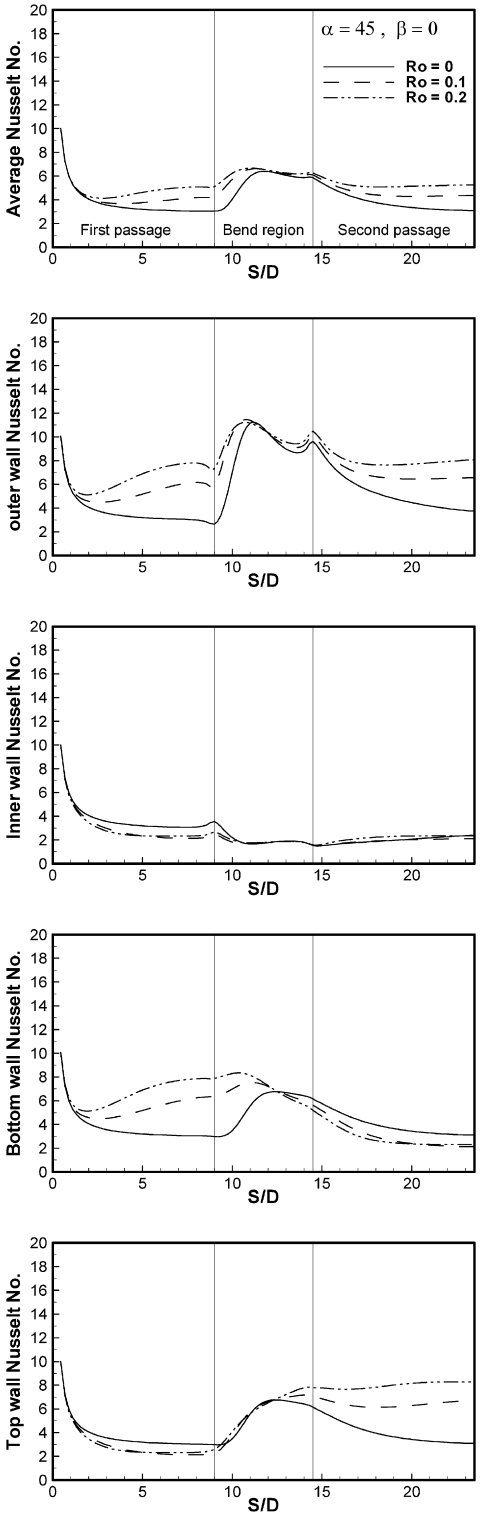

Fig. 12. Average peripheral Nusselt number and each four wall Nusselt number of the duct versus axial distance at $Re = 200$ for rotation axis at angles of $\alpha = 45$ and $\beta = 0$.

the bend region the Nusselt number decreases first and increases beyond the mid-section. Downstream, the Nusselt number variation trend is similar to the first straight passage. The physics of getting thinner or thicker the boundary layers on the outer or inner walls for the positive and negative cases is easily understandable by tracking the core fluid flow directions in the typical corresponding cases of Figs. 4–6.

In the rotation about y-axis (Fig. 11), the Nusselt numbers on the outer and inner walls are higher than the stationary values. Also, the Nusselt number on the bottom wall (top wall)

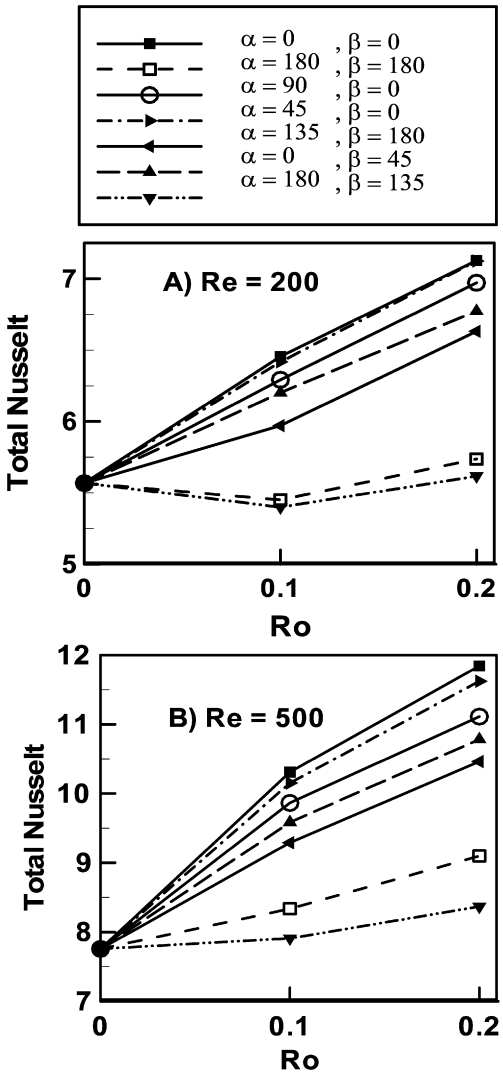

Fig. 13. Total Nusselt number versus rotation number in different rotating cases, (A) $Re = 200$, (B) $Re = 500$.

approaches a higher (low) value than the stationary case at the end of first passage, and then decreases (increases) to a value lower (higher) than the stationary fully developed one. In the rotation at the angles of $\alpha = 45$ and $\beta = 0$ (Fig. 12), the Nusselt number variation on the inner and outer walls behaves similar to the case of $\alpha = \beta = 0$, but on the top and bottom walls, it has the same trend as the case of $\alpha = 90$ and $\beta = 0$ where the values are closer to the stationary case. The same behavior appears in the case of $\alpha = 135$ and $\beta = 180$. In addition, the numerical results obtained for the two more cases of $\alpha = 0$, $\beta = 45$ and $\alpha = 180$, $\beta = 135$ are similar to the cases shown in Figs. 9 and 10, respectively.

To investigate the overall performance of heat transfer rate in the duct for the previously mentioned cases, a total Nusselt number is defined by Eq. (10) using the energy balance for the whole duct

$$Nu = -\frac{Re\,Pr}{4S/D}\ln(T_{\text{wall}} - T_{\text{mean}}) \tag{10}$$

where S/D is the dimensionless axial distance of the duct. Fig. 13 shows different total Nusselt numbers at Re = 200 and $Re = 500$. As shown in this figure, by increasing the Reynolds number, the total Nusselt number increases, and the variation of the total Nusselt number indicates the same trend at different rotation numbers when the axis of rotation is fixed. Regardless of the value of the Reynolds number, the total Nusselt number in the positive rotations is greater than the negative ones. Furthermore, the maximum Nusselt number occurs at the positive rotation with rotation axis orientation of $\alpha = 0$ and $\beta = 0$, and the minimum Nusselt number occurs in the negative rotation with rotation axis orientation of $\alpha = 180$ and $\beta = 135$, where the Coriolis forces and the centrifugal forces act opposite each other in the bend region.

5. Summary and conclusion

A numerical method is performed to study three-dimensional viscous flow and heat transfer in a rotating U-shaped square duct. Non-inertial full Navier–Stokes equations along with the energy equation are solved by a finite volume method based on the SIMPLER algorithm. The effects of the bend region, Reynolds number, rotation number and different rotation directions on the flow field and heat transfer are discussed in detail.

Due to rotation and the bend curvature of the duct, secondary flows are generated as two counter-rotating vortices pushing the maximum axial velocity and cold fluid to the outer wall. Consequently, the boundary layer becomes thinner on the outer, increasing the heat transfer rate, and thicker on the inner wall, decreasing heat transfer rate.

The pattern and strength of secondary flows are strongly dependent on the direction of rotation. The general pattern is a pair of counter-rotating vortices which may break to four or more vortices in higher Reynolds and rotation numbers. Direct influence of these secondary flows is the increase of heat transfer rate on the high pressure side and reduction of it on the low pressure side. The friction factor and the average Nusselt number increases due to rotation. The maximum heat transfer rate occurs when the duct rotates positively about x-axis, while the minimum heat transfer rate takes place in the negative rotation with rotation angles of $\alpha = 180$ and $\beta = 135$.

Acknowledgements

Thanks for the reviewer's time and effort in reviewing my paper and his positive decision regarding my paper.

References

[1] R.K. Shah, A.L. London, Laminar flow forced convection in ducts, in: Advances in Heat Transfer, Academic Press, New York, 1978.
[2] C.G. Speziale, Numerical study of viscous flow in rotating rectangular ducts, J. Fluid Mechanics 122 (1982) 251–271.
[3] C.G. Speziale, The effect of the earth's rotation on channel flow, J. Applied Mechanics 53 (1986) 198–202.
[4] G.J. Hwang, C.Y. Soong, Experimental automation and heat transfer measurement on a rotating thermal system, in: Proc. 3rd Int. Symp. on Transport Phenomena in Thermal Control, 1988, pp. 665–678.
[5] C.Y. Soong, S.T. Lin, G.J. Hwang, An experimental study of convective heat transfer in radially rotating rectangular ducts, in: Collected Papers in Heat Transfer, ASME HTD, vol. 120, 1989.

[6] T.C. Jen, A.S. Lavine, G.J. Hwang, Simultaneously developing laminar convection in rotating isothermal square channels, Int. J. Heat and Mass Transfer 35 (1992) 239–254.
[7] M. Mahadevappa, V.R. Rao, V.M.K. Sastri, Numerical study of steady laminar fully developed fluid flow and heat transfer in rectangular and elliptical ducts rotating about a parallel axis, Int. J. Heat and Mass Transfer 39 (4) (1996) 867–875.
[8] W.R. Dean, The streamline motion of fluid in a curved pipe, Philosophy Magazine 5 (1928) 673–695.
[9] J.J. Hwang, D.Y. Lai, Three-dimensional mixed convection in a rotating multiple pass square channel, Int. J. Heat and Mass Transfer 41 (1998) 979–991.
[10] J.J. Hwang, D.Y. Lai, Three-dimensional laminar flow in a rotating multiple pass square channel with sharp 180-deg turns, J. Fluids Engineering 120 (1998) 488–495.
[11] F. Papa, K. Vaidyanathan, T.J. Keith, K.J. Dewitt, Numerical computations of flow in rotating ducts with strong curvature, Int. J. Numerical Methods for Heat & Fluid Flow 10 (5) (2000) 541–556.
[12] F. Papa, K.J. Dewitt, T.J. Keith, K. Vaidyanathan, Numerical calculation of developing laminar flow in rotating ducts with a 180-deg bend, Int. J. Numerical Methods for Heat & Fluid Flow 12 (7) (2002) 780–799.
[13] S.V. Patankar, Numerical Heat Transfer and Fluid Flow, Hemisphere Pub. Co., 1980.
[14] H.K. Versteeg, W. Malalasekera, An Introduction to Computational Fluid Dynamics: The Finite Volume Method, Longman Scientific & Technical/Wiley, Harlow, Essex, England/New York, 1995.
[15] E.M. Sparrow, Analysis of laminar forced convection heat transfer in the entrance region of flat rectangular ducts, NACA TN 3331, 1955.
[16] H. Schlichting, Boundary Layer Theory, fourth ed., McGraw-Hill, New York, 1960, p. 169.